

## Article

# Simulation Study on Crack Initiation and Energy Mechanisms of Rock-like Samples with Non-Parallel Overlapping Flaws under Uniaxial Compression

Peng Wu <sup>1,2</sup>, Yanlong Chen <sup>1,\*</sup>, Qiang Li <sup>3</sup>, Xianbiao Mao <sup>1</sup>, Lianying Zhang <sup>2</sup>, Ming Li <sup>1</sup>, Liang Chen <sup>4</sup>  
and Zhong Zhao <sup>1,2</sup>

<sup>1</sup> State Key Laboratory for Geomechanics and Deep Underground Engineering, China University of Mining & Technology, Xuzhou 221116, China

<sup>2</sup> Civil Engineering Department, Xuzhou Institute of Technology, Xuzhou 221000, China

<sup>3</sup> School of Resources and Safety Engineering, Chongqing University, Chongqing 400044, China

<sup>4</sup> State Key Laboratory of Coal Resources and Safe Mining, China University of Mining and Technology, Xuzhou 221116, China

\* Correspondence: chenyanlong@cumt.edu.cn

**Abstract:** Non-parallel overlapping flaws widely exist in engineering rock mass. Understanding their crack initiation and energy evolution characteristics is of great significance to ensure the stability of rock engineering. Based on the existing experiments, the influence of flaw inclination angles ( $\beta$ ) on the crack initiation and energy evolution characteristics of rock samples with non-parallel overlapping flaws was studied by numerical simulation. The results show that (1) the uniaxial compressive strength, elastic modulus and crack initiation stress increase with the increase of flaw angle. (2) The boundary energy, strain energy and dissipated energy under peak stress increase with the increase of flaw angle; the dissipated energy increases the most. (3) With the increase of flaw angle, the tension stress zone is transferred to the flaw tip, and the zone is reduced gradually; the maximum tensile stress and the tension stress concentration decrease. (4) In the crack initiation stage, the influence of a lower flaw inclination angle ( $\beta \leq 60^\circ$ ) on the lateral displacement field of the sample is higher than that of a high flaw inclination angle ( $\beta = 75^\circ$ ).

**Keywords:** flaw inclination angle; PFC; mechanical properties; crack initiation; energy mechanism



**Citation:** Wu, P.; Chen, Y.; Li, Q.; Mao, X.; Zhang, L.; Li, M.; Chen, L.; Zhao, Z. Simulation Study on Crack Initiation and Energy Mechanisms of Rock-like Samples with Non-Parallel Overlapping Flaws under Uniaxial Compression. *Appl. Sci.* **2022**, *12*, 10367. <https://doi.org/10.3390/app122010367>

Academic Editor: Arcady Dyskin

Received: 13 August 2022

Accepted: 12 October 2022

Published: 14 October 2022

**Publisher's Note:** MDPI stays neutral with regard to jurisdictional claims in published maps and institutional affiliations.



**Copyright:** © 2022 by the authors. Licensee MDPI, Basel, Switzerland. This article is an open access article distributed under the terms and conditions of the Creative Commons Attribution (CC BY) license (<https://creativecommons.org/licenses/by/4.0/>).

## 1. Introduction

Some rock engineering activities, including coal mining [1–3], underground chamber excavation [4,5] and shale gas exploitation [6,7], generally lead to new rock fractures. Under external loads, the rock mass often begins to crack from the defect position until failure occurs [8–11]. Therefore, it is of great significance to study the crack initiation characteristics and energy evolution of fractured rock mass to ensure the stability of rock mass engineering structure.

To study the crack initiation characteristics of fractured rock, researchers have carried out a large number of laboratory tests, and these tests focus on single flaw [12–16], parallel double flaws [17–20] and non-parallel double flaws [21–23]. For example, through the high-speed photography and acoustic emission (AE) technology, Yang et al. [14] studied the fracture instability process of sandstone with a single flaw and analyzed the effects of flaw inclination angle, length and rock bridge dip angle on crack initiation, crack propagation and the mechanical properties of rock mass. Through the uniaxial compression experiments on Carrara marble with flaws, Wong et al. [16] observed the crack formation by a high-speed camera, analyzed the microscale–macroscale phenomena related to the fracture process of the sample, and distinguished the shear crack and tensile crack. Morgan et al. [19] used a high-speed camera to record the compression failure process of granite samples

with prefabricated parallel double flaws, and analyzed the influence of the geometry of prefabricated flaws on the crack initiation mode. Afolagboye et al. [22] analyzed the influence of flaw inclination angle, flaw length and rock bridge length on crack initiation position and crack propagation with the help of the high-speed camera. Most scholars use high-speed cameras and AE technology to the study cracking mechanisms of rock material with flaws. These methods analyze the influence of crack geometry and external experimental conditions on the crack initiation mode [24–26], and summarize the crack initiation characteristics of fractured rocks (including cracking position, cracking angle and extending direction and crack types) [27–29]. However, because it is difficult to directly measure of stress field inside the sample, most of the studies on the mechanism of crack initiation remain at the macroscopic level.

Compared with laboratory tests, numerical simulation can analyze the crack initiation characteristics from the meso point of view. Cundall et al. [30] proposed a discrete element method (DEM), and simulated rock-like or rock materials by using particles and the contact between particles, and PFC<sup>2D</sup> was developed based on particle discrete element method. Unlike the finite element method, DEM can avoid selecting sophisticated crack initiation criteria and more accurately depict the sample's fracture processes [31,32]. Compared with laboratory experiments, the fracture processes involving crack initiation, coalescence, and propagation of rock can be clearly demonstrated by the breakage of inter-particle bonds in DEM [33], and all numerical data, including those that are difficult or impossible to get directly from laboratory experiments, such as inter-particle contact forces, can be obtained at any stage of simulation [34]. For instance, Yang et al. [35] carried out uniaxial compression tests on red sandstone samples with two non-parallel flaws by using PFC<sup>2D</sup> based on laboratory tests, and revealed the crack evolution mechanism of brittle sandstone samples with two non-parallel flaws through force chain evolution analysis. However, they only performed qualitative analysis and the verification of physical experiments. In recent years, some scholars have paid more attention to the quantitative analysis of crack initiation characteristics of fractured rocks by using stress and displacement fields. Pan et al. [36] studied the effect of flaw length on the initiation characteristics of granite samples with cross double flaws by using PFC<sup>2D</sup>, indicating that the crack initiation position was close to the flaw tip and propagated along the principal stress direction, and the initiation cracks were tensile cracks. Shen et al. [37] discussed the influence of flaw width and flaw inclination angle on the crack initiation angle and crack initiation location of samples with the single flaw by using PFC<sup>2D</sup>, and showed that the crack initiation angle decreased with the increase of flaw width. PFC<sup>2D</sup> can avoid the artificial selection of complex crack initiation criteria to more truly reflect the initiation process of rock-like materials, and it has been developed and extensively used to simulate crack initiation and the propagation of rock-like materials in recent years [38–40].

Moreover, the failure process of rock or rock-like materials is a process from local failure to global failure, and the essence of failure is the nonlinear instability driven by energy [41,42]. Therefore, the analysis of energy evolution characteristics is an important method to reveal the failure characteristics of fractured rocks. Jin et al. [43] studied the influence of inclination angle on the energy evolution characteristics of rock samples with a single flaw by using PFC<sup>2D</sup>, and found that the larger the inclination angle was, more energy was absorbed and dissipated, and the higher the failure degree was. Zhang et al. [44] carried out uniaxial compression tests of rock with a single flaw under different loading rates by using PFC<sup>2D</sup>, and found that energy evolution and failure modes were closely related to loading rates. Most of the research has focused on the influence of loading conditions [44,45], and the geometry of single flaws or parallel flaws [46,47] on the energy evolution characteristics, while studies on the energy evolution characteristics of samples with non-parallel flaws are fewer.

At present, scholars have carried out numerous studies on macroscopic and microscopic mechanical characteristics, crack initiation characteristics and crack evolution laws of rock or rock-like materials with single flaws or parallel flaws. Researches on non-parallel

flaws, especially non-parallel overlapping flaws, mainly use physical test methods to explore their macroscopic mechanical properties and crack propagation characteristics, while the results on their meso-cracking characteristics and energy dissipation laws are fewer. Therefore, in order to make up for the deficiency of this kind of research, based on the laboratory test of Afolagboye et al. [22], PFC<sup>2D</sup> was used to simulate the non-parallel overlapping double flaws of rock-like samples with different inclination angles. From the overall macroscopic mechanical properties, crack initiation stress and deformation field to the local stress field, the crack initiation characteristics of samples with non-parallel overlapping flaws were analyzed, and the failure characteristics are discussed from the aspect of energy evolution.

## 2. Establishment of Numerical Model with Non-Parallel Overlapping Flaws

### 2.1. Selection of Contact Model

The core theory of PFC<sup>2D</sup> is the contact model of particle interaction, in which the parallel bond model (PBM) is commonly used to simulate the mechanical properties of rock-like materials [30,32]. In the PBM, forces and moments can be transferred by applying a bond between particles, which is similar to the distribution of a group of springs with a certain stiffness centered on the contact plane of particles, as shown in Figure 1. After bonding, once the relative motion of particles occurs, the force and bending moment will be generated and the stress state of the medium will be changed.

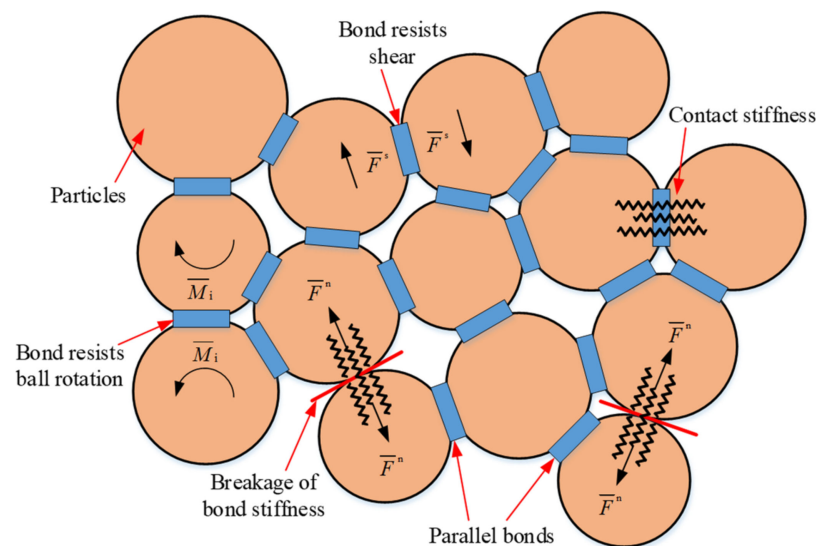


**Figure 1.** Cohesion model and its micromechanical behavior in the PBM [38,48].

According to the different contact forces, the bonding forms between particles can be roughly divided into two categories: one is the contact bonding that can transfer the force between particles, and the other is the parallel bonding that can not only transfer the force but also the torque. The contact bond between particles can be decomposed along the normal and tangent directions of the contact surface.

$$F_i = F^n n_i + F^s t_i \quad (1)$$

where  $F^n$  and  $F^s$  are normal contact force and tangential contact force, respectively, and meet the conditions of  $F^s \leq \zeta F^n$ ;  $\zeta$  is the friction coefficient between particles;  $n_i$  and  $t_i$  are the unit normal vector and tangential vector along the contact surface, respectively.

Each subsequent relative displacement and rotation increment ( $\Delta U^n, \Delta U^s, \Delta \theta^n, \Delta \theta^s$ ) produces an increment of elastic force and moment, which can be calculated from Equation (2) and is added to the current values.

$$\begin{cases} \Delta \bar{F}^n = \bar{k}^n A \Delta U^n \\ \Delta \bar{F}^s = \bar{k}^s A \Delta U^s \\ \Delta \bar{M}^n = -\bar{k}^s J \Delta \theta^n \\ \Delta \bar{M}^s = -\bar{k}^n I \Delta \theta^s \end{cases} \quad (2)$$

where  $A$  is the area of the cross-section parallel to the bond;  $I$  and  $J$  are the moment of inertia and polar moment of inertia of the parallel bonded cross-section;  $\Delta U^n$  and  $\Delta U^s$  are relative displacement increments in normal and tangent directions respectively;  $\Delta \theta^n$  and  $\Delta \theta^s$  are the relative corner increments in the normal and tangent directions respectively. In addition, if the specimen is not subject to tensile shear failure during loading, the maximum tensile stress and tangential stress applied to the parallel bond shall also meet the following conditions:

$$\bar{\sigma}^{\max} = \frac{-\bar{F}^n}{A} + \bar{\beta} \frac{|\bar{M}_b| \bar{R}}{I} < \bar{\sigma}_c \quad (3)$$

$$\bar{\tau}^{\max} = \frac{|\bar{F}^s|}{A} + \bar{\beta} \frac{|\bar{M}_t| \bar{R}}{J} < \bar{\tau}_c \quad (4)$$

where  $\bar{M}_b$  and  $\bar{M}_t$  are bending moment and torque of parallel bonding interface;  $\bar{R}$  is the particle radius used in the calculation;  $\bar{\sigma}_c$  and  $\bar{\tau}_c$  are ultimate compressive strength and shear strength, respectively;  $\bar{\beta}$  is the moment contribution factor.

In PFC<sup>2D</sup>, the parallel bond model can clearly reflect the real failure situation of rock or rock-like materials. Therefore, the parallel bond model was used to simulate the samples with non-parallel overlapping flaws in this study.

In the process of stress, when the maximum tensile stress or tangential stress at the contact exceeds the corresponding limit value, the bonding failure will occur and micro tensile or shear cracks will be formed [48]. When the micro-cracks are continuously formed and connected, macro-cracks will be formed.

### 2.2. Model Generation and Verification

In this study, the numerical simulation experiment was based on the laboratory experiment conducted by Afolagboye et al. [22]. The samples with a size of 152 mm × 76 mm were prepared for the static uniaxial compression test. In PFC<sup>2D</sup>, to reduce the interference of irrelevant factors in numerical simulation, the same random number was selected in all simulations, and the standard model with the same size as the laboratory experiment was established. There were 23,552 particles with a uniform distribution in each intact numerical model, and the particle size ranged from 0.3 mm to 0.5 mm. The sample model with non-parallel overlapping flaws was obtained by deleting particles in the specific area. The flaw length  $2a$  was 12.7 mm, the flaw width  $2b$  was 1.27 mm, the rock bridge length  $L$  was 12.7 mm, and the flaw inclination angle  $\beta$  was set as 15°, 30°, 45° and 60° respectively, as shown in Figure 2.

The loading rate of 0.05 m/s was adopted, the specimen was loaded in a strain-controlled manner by specifying the speeds of the upper and lower walls. Local damping was used and the damping constant was set to 0.7. The axial stress in the numerical model was measured by the average value of the total force applied by the particles to the wall divided by the cross-sectional area of the specimen.

After the establishment of the PFC<sup>2D</sup> numerical model, the micro-parameters of particles and particle bonding should be determined, and its mechanical properties should be consistent with the macro-mechanical response of laboratory physical experiments. At present, researchers mainly use the “trial and error method” to determine the meso parameters [49–51]. Firstly, the macro-elastic modulus of rock-like sample is determined by

the stiffness ratio and meso modulus of the contact model. For a fixed sample model and a given stiffness ratio, the meso modulus can be calibrated by tests. Then, the calibrated meso parameters are fixed, and the bonding parameters are adjusted to match the strength of rock-like sample [33]. Finally, the meso parameters are fine-tuned to match the numerical simulation requirements during the numerical calculation.

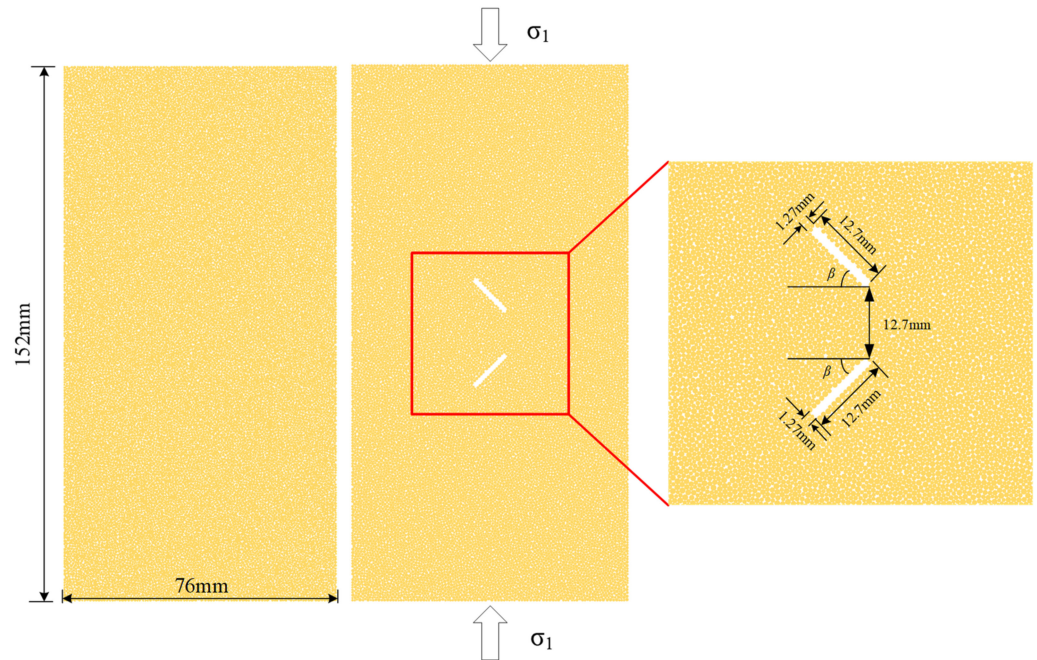


**Figure 2.** Intact numerical model and a numerical model with non-parallel overlapping flaws.

In this study, by repeatedly adjusting the meso parameters of the defect-free sample model, the macro-mechanical parameters were consistent with the laboratory experiments of Afolagboye et al. [22]. Table 1 shows the meso parameters of the sample model, and Table 2 shows the comparison of macro-mechanical parameters.

**Table 1.** Meso parameters of rock-like materials in PFC<sup>2D</sup> model.

Parameters	Value	Remark
Contact bond stiffness ratio	1.2	
Contact bond modulus (GPa)	3.76	
Friction coefficient	0.35	
Parallel bond stiffness ratio	1.2	
Parallel bond modulus (GPa)	3.76	
Parallel bond tension strength, mean (MPa)	17.2	Normal distribution
Parallel bond tension strength, standard deviation (MPa)	2.06	
Parallel bond cohesion, mean (MPa)	28.0	Normal distribution
Parallel bond cohesion, standard deviation (MPa)	3.36	
Parallel bond friction angle (°)	30	

**Table 2.** Comparison of laboratory test results and numerical simulation results.

Type	Density $\rho$ /(g/cm <sup>3</sup> )	Young’s Modulus $E$ /GPa	Uniaxial Compressive Strength $\sigma_c$ /MPa
Experimental results	2.2	7.50	46.35
Simulation results	2.2	7.47	46.32

Based on the calibrated model parameters, a simulation experiment was carried out on the sample with non-parallel overlapping flaws.

Table 3 shows the results of laboratory physical test and simulation results for samples with non-parallel overlapping flaws. From the results, although there are differences between the experimental results and the numerical results, they are still in good agreement generally. The main reasons for the difference are: (1) the size and shape of particles are different from those of real grains; (2) the macroscopic experiment mechanical parameters used to calibrate the meso parameters can only reflect the local characteristics of samples [52]; (3) The numerical simulation is a two-dimensional analysis, which cannot accurately simulate the three-dimensional experimental samples [29].

**Table 3.** Comparison of crack propagation results between laboratory experiment [22] and numerical simulation.

Flaw Inclination Angle/(°)	Diagram of Crack Propagation in Physical Experiments	Diagram of Simulation Results
15		
30		
45		
60		

On this basis, the further simulation experiments on samples with non-parallel overlapping flaws at the flaw inclination angles  $\beta$  of  $15^\circ$ ,  $30^\circ$ ,  $45^\circ$ ,  $60^\circ$  and  $75^\circ$  were carried out.

### 3. Simulation Results and Analysis

#### 3.1. Strength and Deformation Characteristics of Rock-like Samples

Figure 3 shows the results of the axial stress–strain curve of samples with non-parallel overlapping flaws. The numerical simulation results show that the sample with a larger flaw inclination angle has higher uniaxial compressive strength (UCS) and elastic modulus. It is worth noting that the axial stress of the samples with different flaw inclination angles decreases suddenly after reaching the peak value, which indicates that this material is brittle. The analysis results show that there is a close relationship between the flaw inclination angle and the mechanical properties of the rock-like materials with non-parallel overlapping flaws.

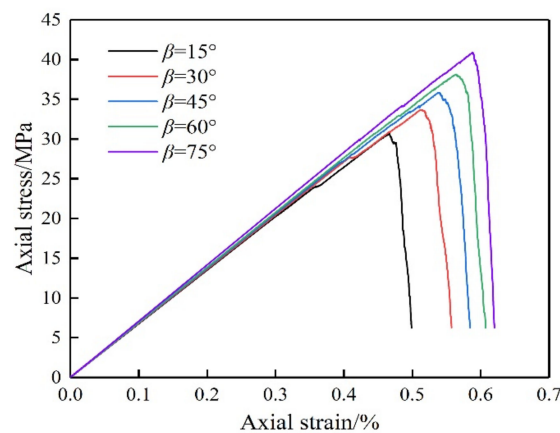


**Figure 3.** Axial stress–strain curves of sample models with different flaw inclination angles.

To quantitatively understand the relationship between UCS, elastic modulus and flaw inclination angle, the numerical simulation results of UCS and elastic modulus changing with flaw inclination angle are shown in Figure 4. It can be seen that the UCS and elastic modulus of the sample increase monotonously with the increase of the flaw inclination angle. When the flaw inclination angle increases from  $15^\circ$  to  $75^\circ$ , the UCS increases by 33.2%, and the elastic modulus increases by 5.5%. Although the changing trend of UCS and elastic modulus with flaw inclination angle is consistent, the UCS is more sensitive to the change of flaw inclination angle. From the overall trend, a large flaw inclination angle can weaken the deterioration effect of non-parallel overlapping flaws on the UCS and elastic modulus of samples.

#### 3.2. Crack Initiation Stress of Rock-like Samples

In PFC<sup>2D</sup>, for an intact sample, the crack initiation stress of an intact sample is difficult to be determined by the number of micro-cracks due to the discrete crack distribution. However, for the samples with defects, the crack initiation usually starts from the existing defects, and the crack initiation stress is defined as the corresponding stress value when the number of micro-cracks reaches about 10% of the total number of cracks under the peak stress of the sample [35]. According to the laboratory test results and numerical simulation results, the variation of crack initiation stress under different flaw inclination angles is shown in Figure 5.

It can be seen that the results of numerical simulation are in good agreement with the results of the uniaxial compression laboratory test performed by Afolagboye et al. [22], and the crack initiation stress increases with the increase of flaw inclination angle.

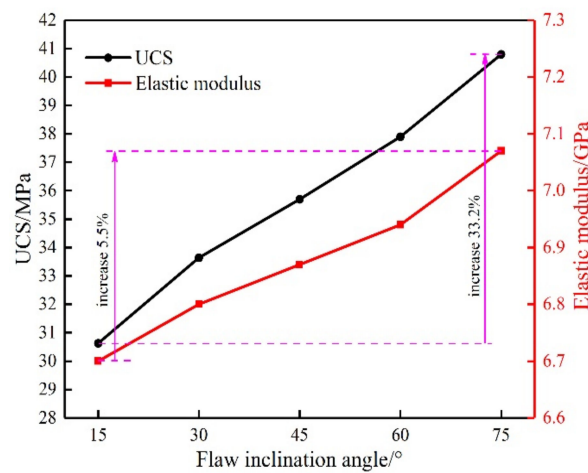


**Figure 4.** Variation of UCS and elastic modulus of a sample model with different flaw inclination angles.

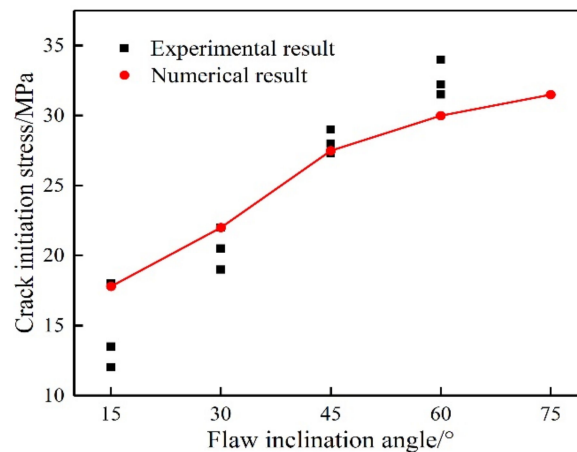


**Figure 5.** Result comparison of laboratory tests and numerical simulation of crack initiation stress.

Figure 6 is a snapshot of different numerical models under crack initiation stress. For the convenience of comparison, the snapshot of the intact sample model was taken when the number of micro-cracks reaches about 10% of the total number of cracks under the peak stress, as shown in Figure 6a. In Figure 6b, if the flaw inclination angle  $\beta = 15^\circ$ , the micro-cracks are all concentrated near the flaw tip. When  $\beta$  increases from  $30^\circ$  to  $60^\circ$ , part of the micro-cracks is generated at the flaw tip, while the other part is dispersed in the model, and the degree of dispersion increases with the increase of flaw inclination angle, as shown in Figure 6c–e. When the flaw inclination angle  $\beta = 75^\circ$ , only a few micro-cracks appear at the flaw tip, and most of them disperse in the sample model, which is similar to the micro-cracks in the intact sample model, as shown in Figure 6a,f. It shows that with the increase of flaw inclination angle, the crack concentration of the model decreases.

### 3.3. Energy Characteristics of Rock-like Samples

According to the law of thermodynamics, the destruction of matter is a kind of instability phenomenon caused by energy evolution. Under the condition of uniaxial compression, the external force does work on the rock, and part of the energy is stored in the rock, which is called strain energy. The other part of the energy is used for the friction of micro-defect closure, crack propagation and relative dislocation of flaw surface in rock, which is called dissipative energy. When the accumulated strain energy of rock reaches a certain threshold, it will be released and transformed into dissipative energy, leading to rock failure.

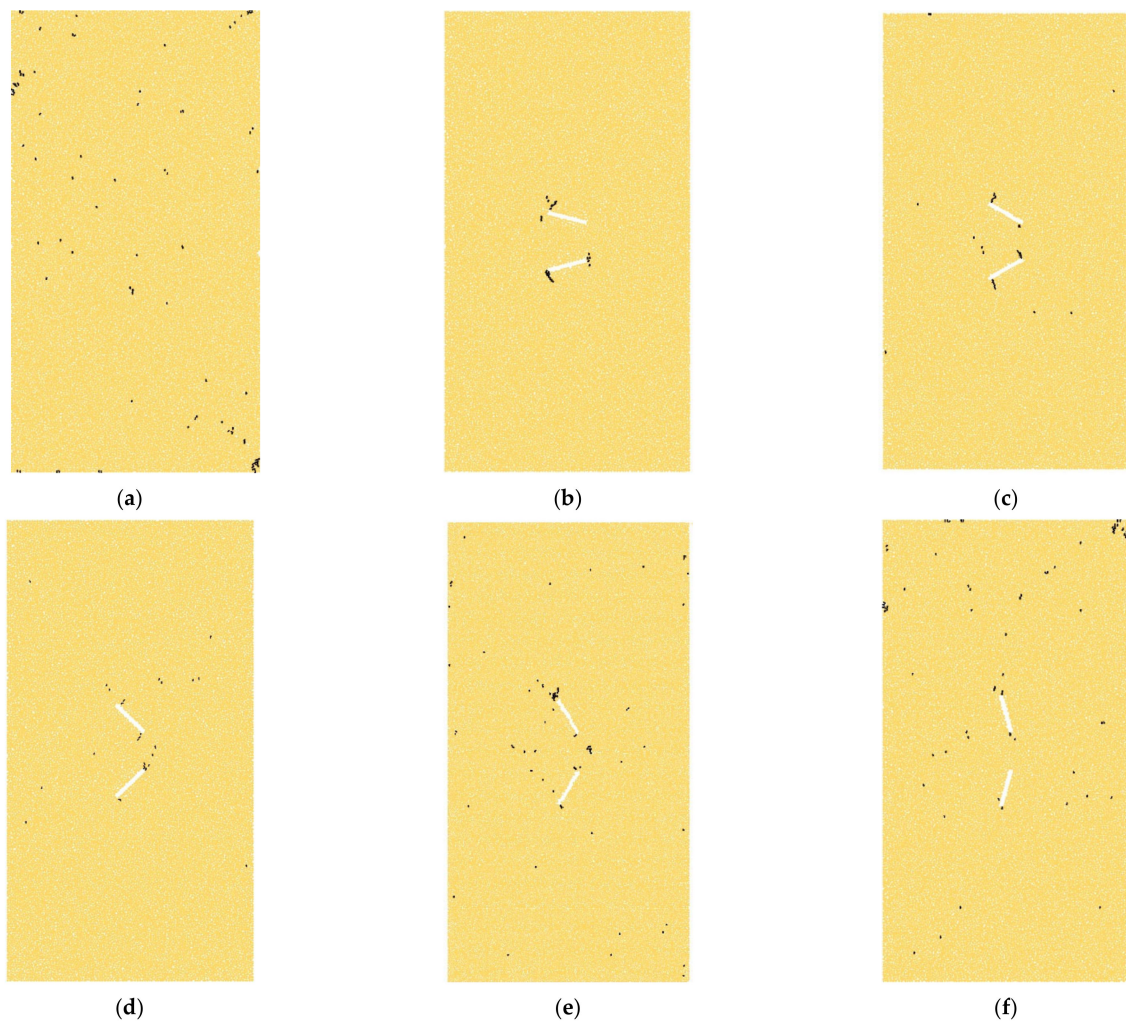


**Figure 6.** Snapshot of different numerical models under crack initiation stress. (a) Intact model; (b)  $\beta = 15^\circ$ ; (c)  $\beta = 30^\circ$ ; (d)  $\beta = 45^\circ$ ; (e)  $\beta = 60^\circ$ ; (f)  $\beta = 75^\circ$ .

In the parallel bonding model, the boundary energy is the total input energy [48]. According to the first law of thermodynamics, there are

$$E = E_d + E_e \quad (5)$$

$$E_e = E_p + E_{pb} \quad (6)$$

where  $E$  is the boundary energy,  $E_d$  is the dissipative energy of the rock,  $E_e$  is the strain energy of the rock,  $E_p$  is the grain strain energy, and  $E_{pb}$  is the parallel bond strain energy.

The system energy monitoring in PFC<sup>2D</sup> can be realized by the built-in fish language. Figure 7 shows the relationship between the variation law of meso energy and the variation law of stress in samples with different flaw inclination angles. It can be found that the meso energy evolution of samples with different flaw inclination angles has similar characteristics. Combined with the characteristic points of the stress–strain curve, it can be roughly divided into three stages. The analysis was performed taking the sample model with the flaw inclination angle  $\beta = 45^\circ$  as an example, as shown in Figure 7d.

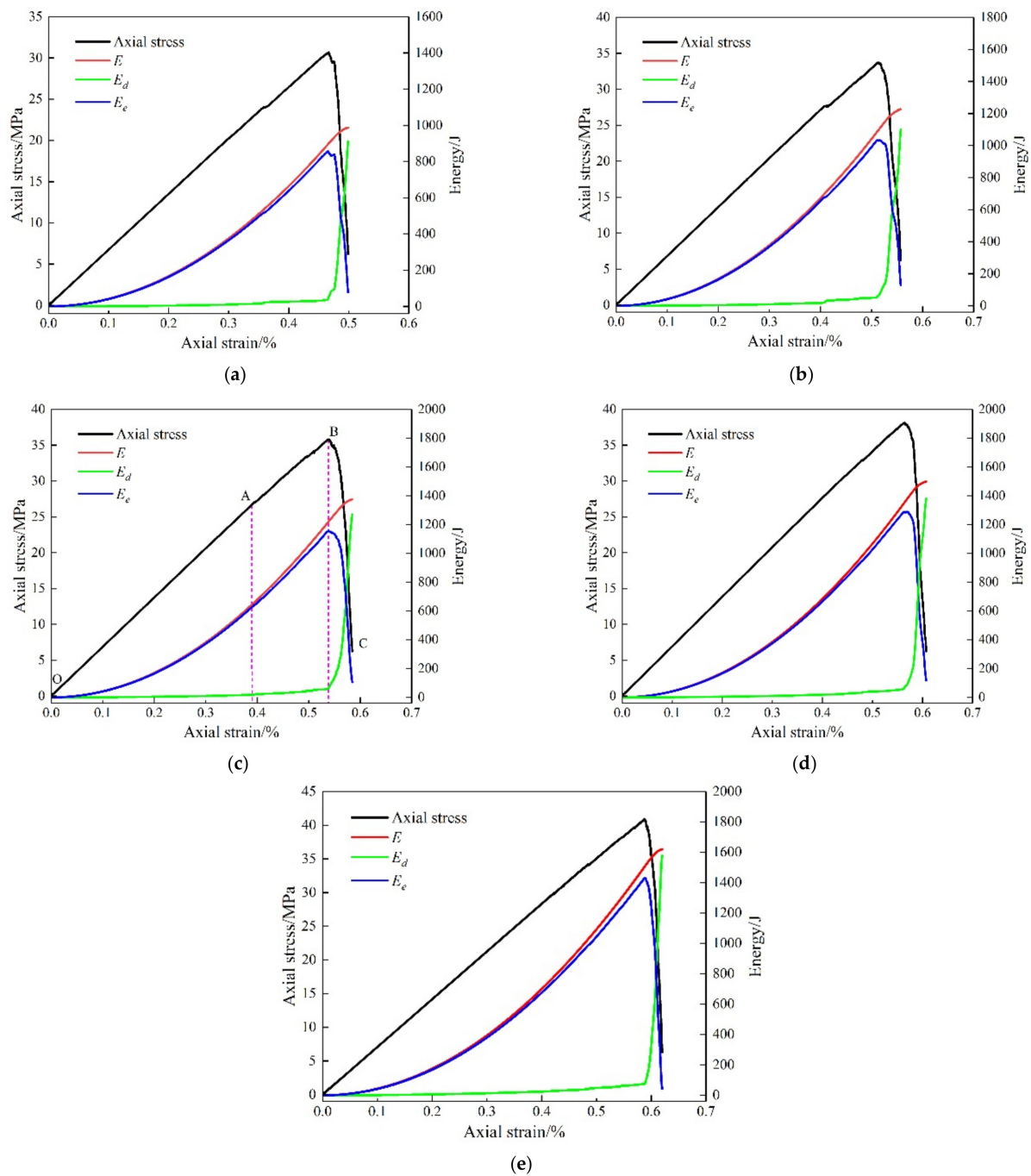


**Figure 7.** Energy evolution of a sample models with different flaw inclination angles. (a)  $\beta = 15^\circ$ ; (b)  $\beta = 30^\circ$ ; (c)  $\beta = 45^\circ$ ; (d)  $\beta = 60^\circ$ ; (e)  $\beta = 75^\circ$ .

According to the analysis of micro energy curve, in stage I (section OA), that is, before the crack initiation stress, the boundary energy and strain energy curves almost overlap, and the dissipated energy is at a low value. It indicates that only a small number of micro-cracks are generated, the internal damage of the sample is small, and the boundary energy is basically stored in the sample in the form of strain energy. In stage II (section AB), when the crack initiation stress is reached, the boundary energy and strain energy continue to increase, but the curves of boundary energy and strain energy begin to separate obviously. Part of the boundary energy is transformed into dissipative energy, and the dissipative energy increases steadily. It indicates that with the continuous work of external force, the bond between particles in the sample is destroyed, which leads to the continuous

generation of micro-cracks and the increase of damage degree in the sample. In stage III (section BC), after the peak stress, the boundary energy continues to increase, and the strain energy is released rapidly and transformed into dissipative energy, which leads to the rapid growth of dissipative energy. When the curves of strain energy and dissipative energy intersect, the dissipative energy occupies the dominant position. It indicates that with the rapid increase of the number of micro-cracks, the micro-cracks further expand and connect, and form a macro flow surface, resulting in the complete loss of the bearing capacity of the sample.

To further analyze the energy evolution characteristics of samples with different flaw inclination angles, the boundary energy, strain energy and dissipated energy of samples with different flaw inclination angles under peak stress are presented in Figure 8. It can be seen that there is an obvious relationship between the flaw inclination angle of the sample and the accumulation and dissipation of energy. With the increase of flaw inclination angle, the peak boundary energy, strain energy and dissipation energy increase approximately linearly.

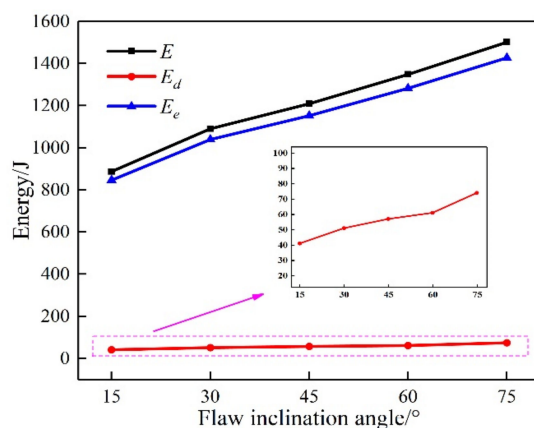


**Figure 8.** Energy variation of sample models with different flaw inclination angles under peak stress.

According to Figure 8 and Table 4, when the flaw inclination angle increases from 15° to 75°, the boundary energy increases by 69.22%, the strain energy increases by 68.68%, and the dissipated energy increases by 80.49%. It can be seen that the dissipative energy increases the most, followed by the boundary energy, and finally the strain energy. This indicates that the energy used for crack initiation, crack propagation and friction between particles increases with the increase of flaw inclination angle. At the same time, the strain energy value increases with the increase of flaw inclination angle, and the proportion of the total energy is relatively stable; the average value is about 95%. It indicates that the ability of storing strain energy between particles increases, but most of the energy in the model is still stored in the form of strain energy under peak stress.

**Table 4.** Variation of energy ratio of sample models with different flaw inclination angles under peak stress.

Flaw Inclination Angle/°	$E/J$	$E_e/J$	$E_d/J$	$E_e/E$	$E_d/E$
15	887	846	41	95.38%	4.62%
30	1090	1034	51	94.86%	5.14%
45	1209	1152	57	95.29%	4.71%
60	1348	1282	61	95.10%	4.90%
75	1501	1427	74	95.07%	4.93%

In addition, the change of dissipated energy is closely related to the generation of micro-cracks. Figure 9 describes the change of the number of micro-cracks with the flaw inclination angle under peak stress. It can be seen that the cracks are mainly tensile-

dominating cracks, and the larger the flaw inclination angle, the more cracks are generated. This is consistent with the variation law of dissipated energy. Therefore, the larger the flaw inclination angle, the more energy consumed for crack generation and propagation, the more serious the internal damage, and the higher the damage degree.

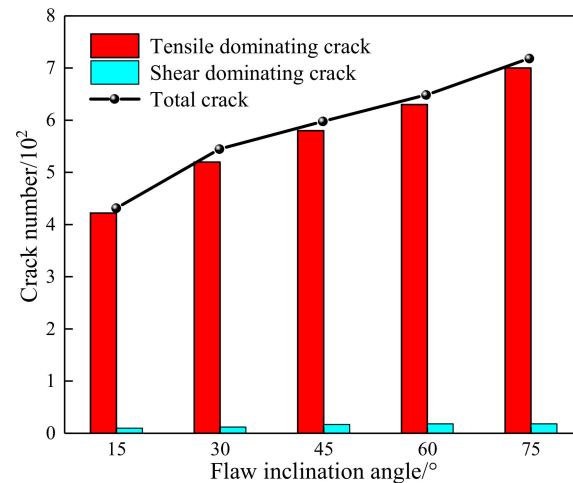


**Figure 9.** The number of cracks in sample models with different flaw inclination angles under peak stress.

## 4. Discussion

### 4.1. Local Stress Characteristics under Crack Initiation Stress

In the previous section, the crack initiation and deformation field of the sample model with different flaw inclination angles were analyzed. The results show that the crack initiation process of samples with different flaw inclination angles has different characteristics. Besides, the crack initiation process of fractured rock or rock-like materials is obviously related to the change of stress field around the flaw [39,51].

Figure 10 shows the parallel bond contact force distribution around the flaw just before reaching the crack initiation stress. In this Figure, the contact force is represented by line segments; green represents tensile force, and red represents compressive force. The width and direction of the line represent the magnitude and direction of the force respectively.

The parallel bond contact force of the intact sample before the crack initiation stress is uniformly distributed in the sample, such as Figure 10a. For the samples with flaws, the distribution of parallel bond force is not uniform, and the distribution characteristics have a great relationship with the flaw inclination angle. When the flaw inclination angle  $\beta = 15^\circ$  in the sample model, the tensile stress is concentrated in the middle of the upper and lower surfaces of the flaw, and the compressive stress is concentrated at the tip of the flaw, as shown in Figure 10b. With the increase of flaw inclination angle, the area of tensile stress concentration on the flaw surface decreases and gradually transfers to the tip of the flaw, while the area of compressive stress concentration at the tip of the flaw gradually extends to the middle of the flaw, as shown in Figure 10c–e. When the flaw inclination angle  $\beta = 75^\circ$ , there is almost no tensile stress concentration on the flaw's surface, and all of them are compressive stress concentration areas, such as in Figure 10f. It shows that the concentration of tensile stress around the flaw decreases with the increase of flaw inclination angle. Due to the stress-shielding effect, there is a low-level parallel bond contact force area between the two flaws, and with the increase of flaw inclination angle, this area gradually decreases until it almost disappears at  $\beta = 75^\circ$ .

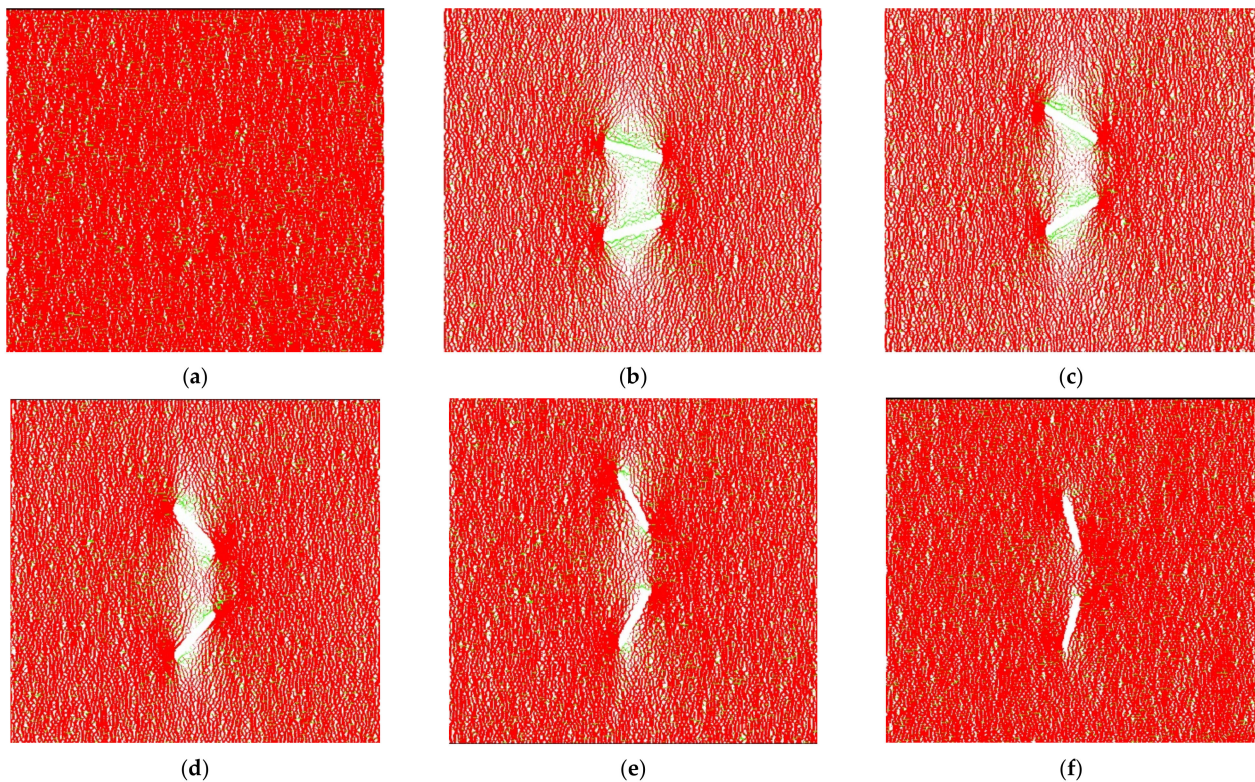


**Figure 10.** Parallel bond force distribution of different models just before crack initiation stress. (a) Intact model; (b)  $\beta = 15^\circ$ ; (c)  $\beta = 30^\circ$ ; (d)  $\beta = 45^\circ$ ; (e)  $\beta = 60^\circ$ ; (f)  $\beta = 75^\circ$ .

Figure 10 reveals the stress distribution around the flaw intuitively, but it still stays at the qualitative level. To realize the quantitative description, the specific stress value should be calculated. In PFC<sup>2D</sup>, the local stress distribution around the flaw can be obtained by setting a series of measuring circles to monitor the average stress in the area to be measured. Because of the discreteness of the PFC<sup>2D</sup> model, the diameter of the measuring circle is too large or too small, which will cause the error of stress measurement. According to the research results of Liu et al. [51] and Fan et al. [53], the measured stress value is more accurate when each measurement circle area contains about 15 particles. Because the cracks and loading conditions are symmetrical in the experiment, the upper cracks were mainly studied here. In this model, a total of 12 measuring circles with a radius of 1.27 mm was set, which were distributed around the flaw. Their positions and numbers are shown in Figure 11.

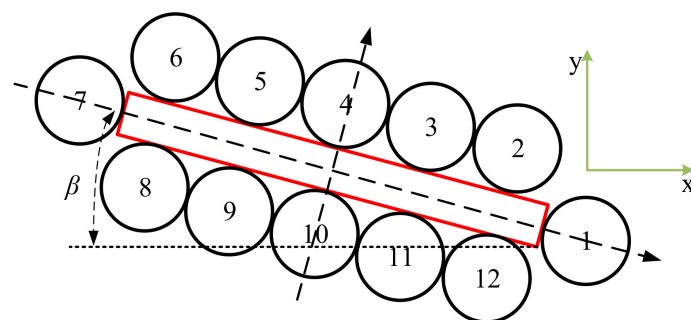


**Figure 11.** Layout of measuring circles.

In PFC<sup>2D</sup>, the average stress monitored by measuring circles can only be expressed in the form of components. According to the elastic mechanics, the maximum principal stress ( $\sigma_1$ ) and the minimum principal stress ( $\sigma_3$ ) at different locations of the flaw are calculated by the detected stress components to further understand the change of local stress around the flaw under the crack initiation stress. In order to keep up with the traditional geotechnical engineering field, the compressive stress is positive and the tensile stress is negative in this section.

Figure 12 shows the distribution maps of the maximum and minimum principal stresses around the flaw under different model initiation stresses. The distribution patterns of  $\sigma_1$  and  $\sigma_3$  around the flaws are quite different at different flaw inclination angles. When the flaw inclination angle  $\beta = 15^\circ$ ,  $\sigma_1$  and  $\sigma_3$  on the upper surface of the flaw are greater than those on the lower surface of the flaw due to the stress-shielding effect. The maximum value of  $\sigma_1$  and  $\sigma_3$  appears in M1 and M7 (flaw tip);  $\sigma_1$  of the 12 measuring circles are all positive values, the  $\sigma_1$  in the middle part of the upper and lower surfaces of the flaw is positive at a low level, and the lowest value of  $\sigma_1$  appears in M4 and M10. The  $\sigma_3$  measured at the flaw tip is a positive value, and the  $\sigma_3$  measured on the upper and lower surfaces of the flaw is negative. When  $\beta = 30^\circ$ , the stress-shielding effect is still obvious; the greatest values of  $\sigma_1$  and  $\sigma_3$  also appear in M1 and M7 and the lowest value of  $\sigma_1$  appears in M5 and M11. When  $\beta = 45^\circ$ , the stress-shielding effect is weakened, and the least value of  $\sigma_1$  appears in M6 and M12. When  $\beta = 60^\circ$ , the stress-shielding effect almost disappears; the greatest values of  $\sigma_1$  and  $\sigma_3$  appear in M2 and M8, which is different from the above results; the distribution of  $\sigma_3$  is in a round shape. When  $\beta = 75^\circ$ , the difference between the values of  $\sigma_1$  is small, and the distribution  $\sigma_3$  at  $\beta = 75^\circ$  is similar to that at  $\beta = 60^\circ$ .

In a word, when the flaw inclination angle  $\beta$  increases from  $15^\circ$  to  $75^\circ$ , the shape of the maximum principal stress  $\sigma_1$  changes from a flat to a proximal circular shape; the greatest value moves from the flaw tip to the adjacent position in a counter-clockwise direction, but it is still near the flaw tip; the lowest value moves from the middle of the flaw to the flaw tip in a counter-clockwise direction; the distribution and change of the minimum principal stress  $\sigma_3$  is similar to that of  $\sigma_1$ . It shows that with the increase of flaw inclination angle, the concentration effect of tensile stress and compressive stress around the flaw decreases gradually.

According to the experimental results of Wong et al. [16], the initial flaw of rock or rock-like material with defects is usually tensile cracking, which is essentially caused by tensile stress. As shown in Figures 10 and 12, the tensile stress concentration occurs on both sides of the flaw, and the initial crack initiation is in the tensile stress zone. To further analyze the influence of flaw inclination angle on crack initiation, the variation graphs of maximum tensile stress of samples with different flaw inclination angles were plotted, as shown in Figure 13. The maximum tensile stress decreases gradually with the increase of flaw inclination angle, which is opposite to the change of crack initiation stress. This shows that the larger the flaw inclination angle, the lower the concentration of tensile stress, and the more difficult the cracking at the flaw tip is.

#### 4.2. Lateral Displacement Characteristics under Crack Initiation Stress

The displacement field of rock-like material samples changes with the evolution of micro-crack distribution. Under the condition of uniaxial compression, the lateral displacement of rock-like materials occurs. This kind of material is more sensitive to lateral displacement in the process of deformation and failure due to its weak tensile resistance [43]. Therefore, the lateral displacement field of rock-like materials with non-parallel overlapping flaws is analyzed in this section.

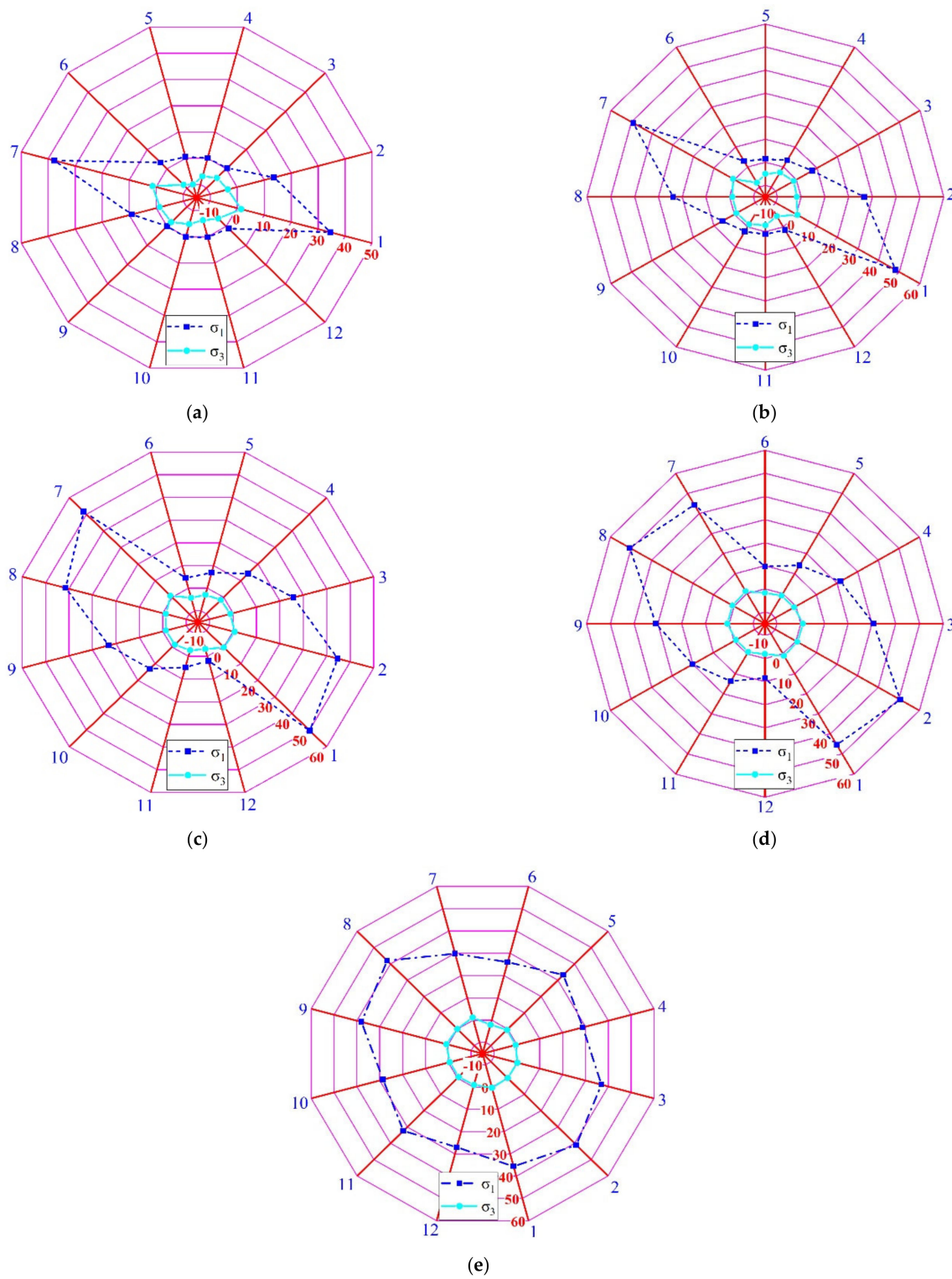


**Figure 12.** The principal stress distribution around flaw under the crack initiation stress in different models (Unit: MPa). (a)  $\beta = 15^\circ$ ; (b)  $\beta = 30^\circ$ ; (c)  $\beta = 45^\circ$ ; (d)  $\beta = 60^\circ$ ; (e)  $\beta = 75^\circ$ .

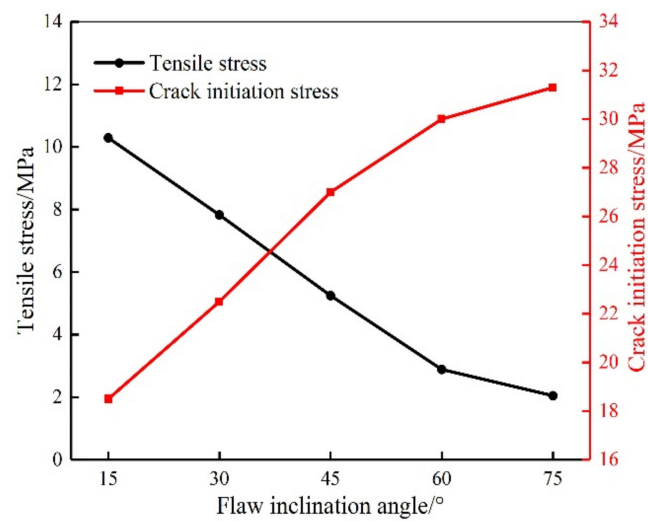


**Figure 13.** Variation of the maximum tensile stress around the flaw and the crack initiation stress with the flaw inclination angle.

Figure 14 shows the contour map of the lateral displacement of different numerical models under the crack initiation stress, and different colors represent different lateral displacements. The contour map of the intact sample model generally presents uniform strip distribution, as shown in Figure 14a. However, the numerical model with different flaw inclination angles shows different characteristics. The contour map presents non-uniform and symmetrical distribution. The contour of lateral deformation deflects near the flaw and concentrates on the flaw surface. The contour is more concentrated near the flaw tip, and the number of the contour increases with the increase of flaw inclination angle. The maximum lateral displacement near the flaw tip increases with the increase of flaw inclination angle from  $15^\circ$  to  $60^\circ$ . When the flaw inclination angle  $\beta = 45^\circ$  and  $\beta = 60^\circ$ , the maximum lateral displacement near the flaw tip is close to the maximum lateral displacement of the model, such as in Figure 14d,e. It indicates that the lateral displacement field under crack initiation stress is greatly affected. In Figure 14f, the maximum lateral displacement around the flaw and the concentration degree of contour around the flaw at  $\beta = 75^\circ$  are lower than those at  $\beta = 15^\circ$ . Therefore, the influence on the lateral displacement field is small at  $\beta = 75^\circ$ . Due to the existence of flaws, the area of the lower lateral displacement in the overlapping zone between flaws is generated, and the contour converges to the middle of the upper and lower flaws, presenting a shape of a multi-layer arc; the average curvature radius of the contour increases with the increase in flaw inclination angle.

It can be seen that the influence of non-parallel overlapping flaws on the lateral displacement of the sample surface is mainly concentrated near the flaw. When the flaw inclination angle  $\beta \leq 60^\circ$ , the lateral displacement field near the flaw is obviously affected. In addition, the lateral displacement near the flaw tip has a maximum value and a large variation range, for which it is easy to induce micro-cracks. When the flaw inclination angle  $\beta = 75^\circ$ , the lateral displacement field near the flaw is less affected, the variation range of the lateral displacement near the flaw tip is relatively small, and micro-cracks are difficult to be produced. This may also explain that only a few cracks appear at the flaw tip at  $\beta = 75^\circ$ .

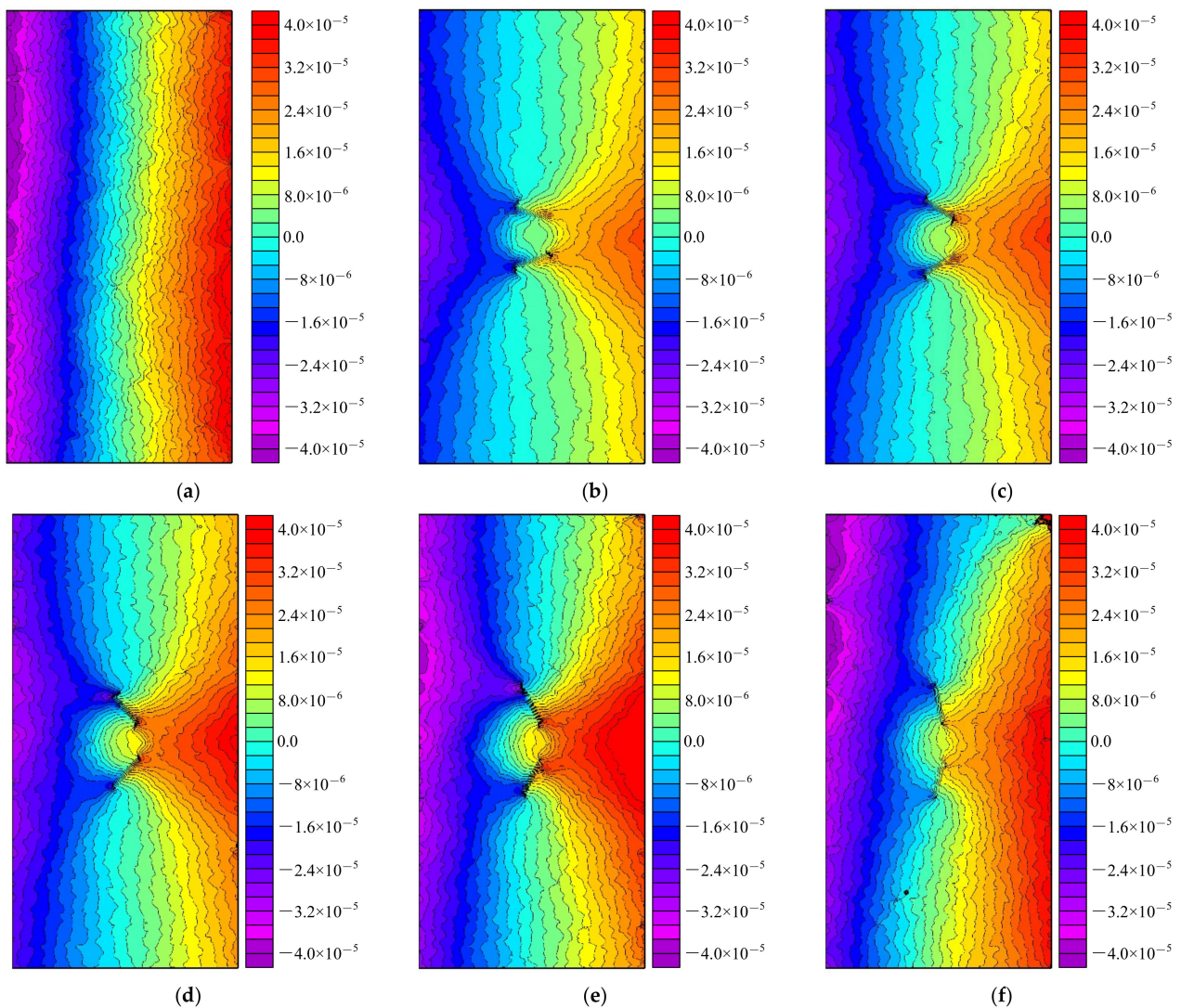


**Figure 14.** The lateral displacement field of different numerical models under crack initiation stress (Unit: m). (a) Intact model; (b)  $\beta = 15^\circ$ ; (c)  $\beta = 30^\circ$ ; (d)  $\beta = 45^\circ$ ; (e)  $\beta = 60^\circ$ ; (f)  $\beta = 75^\circ$ .

## 5. Conclusions

Based on the existing laboratory experiments, a numerical model with non-parallel overlapping flaws was established in this study. It was verified that the numerical model could more truly reflect the crack propagation process. Besides the influence of flaw inclination angle on mechanical properties, crack initiation characteristics and energy evolution was studied.

(1) The results show that for the sample model containing non-parallel overlapping flaws, the UCS and elastic modulus increase monotonously with the increase of flaw inclination angle, and the UCS is more sensitive to the change of flaw inclination angle. The larger the dip angle, the greater the initiation stress, and the lower the crack concentration generated near the flaw.

(2) The boundary energy, strain energy and dissipated energy under peak stress increase with the increase of flaw inclination angle. The dissipated energy increases the most, followed by the boundary energy and finally the strain energy. Combined with the statistics of the number of micro-cracks, it shows that the larger the flaw inclination angle, the more serious the internal damage and the higher the damage degree.

(3) In the early stage of crack initiation, the range of tensile stress zone on the upper and lower surfaces of the flaw decreases with the increase of the flaw inclination angle, and gradually transfers to the flaw tip, while the compressive stress area gradually expands

from the flaw tip to the middle of the flaw. Due to the stress-shielding effect, a low-stress area appears in the flaw overlapping area, and with the increase of flaw inclination angle, this area gradually decreases until it disappears. The distribution pattern of  $\sigma_1$  and  $\sigma_3$  around the flaw gradually changes from flat to proximal circular with the increase of the flaw inclination angle, the stress concentration effect around the flaw weakens, and the maximum tensile stress under the crack initiation stress decreases gradually. This is also the reason for the difficult crack initiation at the flaw tip and the gradually dispersed distribution of cracks under the large flaw inclination angle.

(4) In the crack initiation stage, the effect of the flaw inclination angle on the lateral displacement field is mainly located at the middle of a specimen. When the flaw inclination angle is from  $15^\circ$  to  $60^\circ$ , the lateral displacement field near the flaw is affected significantly. Meanwhile, the lateral displacement of particles in the small area near the flaw tip changes greatly, which makes it easy to induce micro-cracks. When the flaw inclination angle is  $75^\circ$ , the lateral displacement field near the flaw is less affected than other flaw inclination angles.

**Author Contributions:** Conceptualization, P.W. and Y.C.; methodology, Q.L.; validation, Y.C.; formal analysis, P.W.; investigation, P.W.; resources, L.C. and Z.Z.; data curation, M.L.; writing—original draft preparation, P.W.; writing—review and editing, P.W.; visualization, Q.L.; supervision, X.M.; project administration, L.Z.; funding acquisition, Y.C. All authors have read and agreed to the published version of the manuscript.

**Funding:** This work was financially supported by the National Key R&D Program of China (2022YFC2903902) and National Natural Science Foundation of China (51974295).

**Institutional Review Board Statement:** Not applicable.

**Informed Consent Statement:** Not applicable.

**Data Availability Statement:** All data, models, or codes that support the findings of this study are available from the corresponding author upon reasonable request.

**Conflicts of Interest:** The authors declare no conflict of interest.

## References

1. Hebblewhite, B. Fracturing, caving propagation and influence of mining on groundwater above longwall panels—a review of predictive models. *Int. J. Min. Sci. Technol.* **2020**, *30*, 49–54. [[CrossRef](#)]
2. Li, X.; Li, Q.; Hu, Y. Evolution Characteristics of Mining Fissures in Overlying Strata of Stope after Converting from Open-Pit to Underground. *Arab. J. Geosci.* **2021**, *14*, 2795. [[CrossRef](#)]
3. Tian, J.; Xu, D.; Liu, T. An experimental investigation of the fracturing behaviour of rock-like materials containing two V-shaped parallelogram flaws. *Int. J. Min. Sci. Technol.* **2020**, *30*, 777–783. [[CrossRef](#)]
4. Guo, S.; Qi, S.; Ming, C. Influence of tunnel wall roughness and localized stress concentrations on the initiation of brittle spalling. *Bull. Eng. Geol. Environ.* **2015**, *75*, 1597–1607. [[CrossRef](#)]
5. Chen, Z.; Li, X.; Weng, L.; Wang, S.; Dong, L.; Perera, M.S.A. Influence of Flaw Inclination Angle on Unloading Responses of Brittle Rock in Deep Underground. *Geofluids* **2019**, *2019*, 1–16. [[CrossRef](#)]
6. Figueiredo, B.; Tsang, C.F.; Rutqvist, J.; Niemi, A. The effects of nearby fractures on hydraulically induced fracture propagation and permeability changes. *Eng. Geol.* **2017**, *228*, 197–213. [[CrossRef](#)]
7. Da Silva, B.G.; Einstein, H. Physical processes involved in the laboratory hydraulic fracturing of granite: Visual observations and interpretation. *Eng. Fract. Mech.* **2018**, *191*, 125–142. [[CrossRef](#)]
8. Chen, Y.; Cui, H.; Pu, H.; Wu, P.; Chen, L.; Zhang, K. Study on Mechanical Properties and Cracking Mode of Coal Samples under Compression-Shear Coupled Load Considering the Effect of Loading Rate. *Appl. Sci.* **2020**, *10*, 7082. [[CrossRef](#)]
9. Fan, X.; Kulatilake, P.H.S.W.; Chen, X. Mechanical behavior of rock-like jointed blocks with multi-non-persistent joints under uniaxial loading: A particle mechanics approach. *Eng. Geol.* **2015**, *190*, 17–32. [[CrossRef](#)]
10. Cao, R.-H.; Cao, P.; Fan, X.; Xiong, X.; Lin, H. An Experimental and Numerical Study on Mechanical Behavior of Ubiquitous-Joint Brittle Rock-Like Specimens Under Uniaxial Compression. *Rock Mech. Rock Eng.* **2016**, *49*, 4319–4338. [[CrossRef](#)]
11. Cheng, X. Damage and failure characteristics of rock similar materials with pre-existing cracks. *Int. J. Coal Sci. Technol.* **2019**, *6*, 505–517. [[CrossRef](#)]
12. Xu, Y.; Dai, F.; Zhao, T.; Xu, N.; Liu, Y. Fracture Toughness Determination of Cracked Chevron Notched Brazilian Disc Rock Specimen via Griffith Energy Criterion Incorporating Realistic Fracture Profiles. *Rock Mech. Rock Eng.* **2016**, *49*, 3083–3093. [[CrossRef](#)]

13. Dai, F.; Xu, Y.; Zhao, T.; Xu, N.; Liu, Y. Loading-rate-dependent progressive fracturing of cracked chevron-notched Brazilian disc specimens in split Hopkinson pressure bar tests. *Int. J. Rock Mech. Min. Sci.* **2016**, *88*, 49–60. [[CrossRef](#)]
14. Yang, S.Q.; Jing, H.W. Strength failure and crack coalescence behavior of brittle sandstone samples containing a single fissure under uniaxial compression. *Int. J. Fract.* **2011**, *168*, 227–250. [[CrossRef](#)]
15. Zhang, X.; Zhang, Q.; Wu, S. Acoustic emission characteristics of the rock-like material containing a single flaw under different compressive loading rates. *Comput. Geotech.* **2017**, *83*, 83–97. [[CrossRef](#)]
16. Wong, L.N.Y.; Xiong, Q. A Method for Multiscale Interpretation of Fracture Processes in Carrara Marble Specimen Containing a Single Flaw Under Uniaxial Compression. *J. Geophys. Res. Solid Earth* **2018**, *123*, 6459–6490. [[CrossRef](#)]
17. Zhao, Y.; Gao, Y.; Wu, S. Influence of different concealment conditions of parallel double flaws on mechanical properties and failure characteristics of brittle rock under uniaxial compression. *Theor. Appl. Fract. Mech.* **2020**, *109*, 102751. [[CrossRef](#)]
18. Yin, P.; Wong, R.H.C.; Chau, K.T. Coalescence of two parallel pre-existing surface cracks in granite. *Int. J. Rock Mech. Min. Sci.* **2014**, *68*, 66–84. [[CrossRef](#)]
19. Morgan, S.P.; Johnson, C.A.; Einstein, H.H. Cracking processes in Barre granite: Fracture process zones and crack coalescence. *Int. J. Fract.* **2013**, *180*, 177–204. [[CrossRef](#)]
20. Hu, J.; Wen, G.; Lin, Q.; Cao, P.; Li, S. Mechanical properties and crack evolution of double-layer composite rock-like specimens with two parallel fissures under uniaxial compression. *Theor. Appl. Fract. Mech.* **2020**, *108*, 102610. [[CrossRef](#)]
21. Pan, W.; Wang, X.; Liu, Q.; Yuan, Y.; Zuo, B. Non-parallel double-crack propagation in rock-like materials under uniaxial compression. *Int. J. Coal Sci. Technol.* **2019**, *6*, 372–387. [[CrossRef](#)]
22. Afolagboye, L.O.; He, J.; Wang, S. Experimental study on cracking behaviour of moulded gypsum containing two non-parallel overlapping flaws under uniaxial compression. *Acta Mech. Sin.* **2017**, *33*, 394–405. [[CrossRef](#)]
23. Yang, S.Q.; Liu, X.; Jing, H. Experimental investigation on fracture coalescence behavior of red sandstone containing two unparallel fissures under uniaxial compression. *Int. J. Rock Mech. Min. Sci.* **2013**, *63*, 82–92. [[CrossRef](#)]
24. Zhao, Y.; Wang, Y.; Wang, W.; Tang, L.; Liu, Q.; Cheng, G. Modeling of rheological fracture behavior of rock cracks subjected to hydraulic pressure and far field stresses. *Theor. Appl. Fract. Mech.* **2019**, *101*, 59–66. [[CrossRef](#)]
25. Cao, R.-H.; Cao, P.; Lin, H.; Fan, X.; Zhang, C.; Liu, T. Crack Initiation, Propagation, and Failure Characteristics of Jointed Rock or Rock-Like Specimens: A Review. *Adv. Civ. Eng.* **2019**, *2019*, 1–31. [[CrossRef](#)]
26. Sagong, M.; Bobet, A. Coalescence of multiple flaws in a rock-model material in uniaxial compression. *Int. J. Rock Mech. Min. Sci.* **2002**, *39*, 229–241. [[CrossRef](#)]
27. Wong, L.N.Y.; Einstein, H.H. Systematic evaluation of cracking behavior in specimens containing single flaws under uniaxial compression. *Int. J. Rock Mech. Min. Sci.* **2009**, *46*, 239–249. [[CrossRef](#)]
28. Zhang, X.; Liu, Q.; Wu, S.; Tang, X. Crack coalescence between two non-parallel flaws in rock-like material under uniaxial compression. *Eng. Geol.* **2015**, *199*, 74–90. [[CrossRef](#)]
29. Lee, H.; Jeon, S. An experimental and numerical study of fracture coalescence in pre-cracked specimens under uniaxial compression. *Int. J. Solids Struct.* **2011**, *48*, 979–999. [[CrossRef](#)]
30. Cundall, P.A.; Strack, O.D.L. A discrete numerical model for granular assemblies. *Géotechnique* **1979**, *29*, 47–65. [[CrossRef](#)]
31. Peng, F.; Wei, M.; Feng, D.; Ran, T.; Qiu, H.; Gong, J. DEM investigation on the mechanical behaviors of flawed specimens subjected to coupled static-dynamic loads. *Soil Dyn. Earthq. Eng.* **2020**, *135*, 106220.
32. Cundall, P.A.; Potyondy, D.O. A bonded-particle model for rock. *Int. J. Rock Mech. Min. Sci.* **2004**, *41*, 1329–1364.
33. Liu, Y.; Dai, F.; Zhao, T.; Xu, N. Numerical investigation of the dynamic properties of intermittent jointed rock models subjected to cyclic uniaxial compression. *Rock Mech. Rock Eng.* **2017**, *50*, 89–112. [[CrossRef](#)]
34. Du, H.; Dai, F.; Xu, Y.; Liu, Y.; Xu, H. Numerical investigation on the dynamic strength and failure behavior of rocks under hydrostatic confinement in SHPB testing. *Int. J. Rock Mech. Min. Sci.* **2018**, *108*, 43–57. [[CrossRef](#)]
35. Yang, S.Q.; Huang, Y.H.; Jing, H.W.; Liu, X.R. Discrete element modeling on fracture coalescence behavior of red sandstone containing two unparallel fissures under uniaxial compression. *Eng. Geol.* **2014**, *178*, 28–48. [[CrossRef](#)]
36. Pan, H.; Yin, D.; Jiang, N.; Xia, Z.; Kong, H. Crack Initiation Behaviors of Granite Specimens Containing Crossing-Double-Flaws with Different Lengths under Uniaxial Loading. *Adv. Civ. Eng.* **2020**, *2020*, 8871335. [[CrossRef](#)]
37. Shen, J.; Zhan, S.; Karakus, M.; Zuo, J. Effects of flaw width on cracking behavior of single-flawed rock specimens. *Bull. Eng. Geol. Environ.* **2021**, *80*, 1701–1711. [[CrossRef](#)]
38. Shi, H.; Song, L.; Chen, W.; Zhang, H.; Wang, G.; Yuan, G.; Zhang, W.; Chen, G.; Wang, Y.; Lin, G. New non-destructive method for testing the strength of cement mortar material based on vibration frequency of steel bar: Theory and experiment. *Constr. Build. Mater.* **2020**, *262*, 120931. [[CrossRef](#)]
39. Zhang, J.; Zhou, X.; Zhu, J.; Xian, C.; Wang, Y. Quasi-static fracturing in double-flawed specimens under uniaxial loading: The role of strain rate. *Int. J. Fract.* **2018**, *211*, 75–102. [[CrossRef](#)]
40. Castro-Filgueira, U.; Alejano, L.R.; Arzúa, J.; Ivars, D.M. Sensitivity Analysis of the Micro-Parameters Used in a PFC Analysis Towards the Mechanical Properties of Rocks. *Procedia Eng.* **2017**, *191*, 488–495. [[CrossRef](#)]
41. Xie, H.P.; Peng, R.D.; Ju, Y.; Zhou, H.W. On energy analysis of rock failure. *J. Rock Mech. Eng.* **2005**, *24*, 2603–2608.
42. Xie, H.P.; Peng, R.D.; Ju, Y. Energy dissipation of rock deformation and fracture. *J. Rock Mech. Eng.* **2004**, *23*, 3565–3570.
43. Jin, J.; Cao, P.; Chen, Y.; Pu, C.; Mao, D.; Fan, X. Influence of single flaw on the failure process and energy mechanics of rock-like material. *Comput. Geotech.* **2017**, *86150–86162*. [[CrossRef](#)]

44. Zhang, Y.; Wang, G.; Jiang, Y.; Wang, S.; Zhao, H.; Jing, W. Acoustic Emission Characteristics and Failure Mechanism of Fractured Rock under Different Loading Rates. *Shock. Vib.* **2017**, *2017*, 5387459. [[CrossRef](#)]
45. Huang, Y.; Yang, S.; Zeng, W. Experimental and numerical study on loading rate effects of rock-like material specimens containing two unparallel fissures. *J. Cent. South Univ.* **2016**, *23*, 1474–1485. [[CrossRef](#)]
46. Li, D.; Han, Z.; Sun, X.; Zhou, T.; Li, X. Dynamic Mechanical Properties and Fracturing Behavior of Marble Specimens Containing Single and Double Flaws in SHPB Tests. *Rock Mech. Rock Eng.* **2019**, *52*, 1623–1643. [[CrossRef](#)]
47. Zheng, L.; Huang, D.; Li, X.; Hu, X.; Tang, Y. Numerical Analysis of Fracture Behaviour on Marble Samples Containing Two Flaws. *Adv. Civ. Eng.* **2020**, *2020*, 1–15. [[CrossRef](#)]
48. Cho, N.; Martin, C.D.; Segol, D.C. A clumped particle model for rock. *Int. J. Rock Mech. Min. Sci.* **2007**, *44*, 997–1010. [[CrossRef](#)]
49. Shi, H.; Zhang, H.; Song, L.; Yang, Z.; Yuan, G.; Xue, X.; Wang, Y. Failure characteristics of sandstone specimens with randomly distributed pre-cracks under uniaxial compression. *Environ. Earth Sci.* **2020**, *79*, 1–21. [[CrossRef](#)]
50. Yang, S.; Tian, W.; Huang, Y.; Ranjith, P.G.; Ju, Y. An Experimental and Numerical Study on Cracking Behavior of Brittle Sandstone Containing Two Non-coplanar Fissures Under Uniaxial Compression. *Rock Mech. Rock Eng.* **2016**, *49*, 1497–1515. [[CrossRef](#)]
51. Liu, T.; Lin, B.; Yang, W.; Zou, Q.; Kong, J.; Yan, F. Cracking Process and Stress Field Evolution in Specimen Containing Combined Flaw Under Uniaxial Compression. *Rock Mech. Rock Eng.* **2016**, *49*, 3095–3113. [[CrossRef](#)]
52. Donzé, F.V.; Richefeu, V.; Magnier, S. Advances in discrete element method applied to soil rock and concrete mechanics. *Electron. J. Geol. Eng.* **2009**, *8*, 1–44.
53. Fan, X.; Li, K.; Lai, H.; Xie, Y.; Cao, R.; Zheng, J. Internal stress distribution and cracking around flaws and openings of rock block under uniaxial compression: A particle mechanics approach. *Comput. Geotech.* **2018**, *102*, 28–38. [[CrossRef](#)]